

DETECTING PLANETS AROUND VERY LOW MASS STARS WITH THE RADIAL VELOCITY METHOD

A. REINERS^{1,3}, J. L. BEAN^{1,4}, K. F. HUBER², S. DREIZLER¹, A. SEIFAHRT¹, & S. CZESLA²
Draft version February 13, 2022

ABSTRACT

The detection of planets around very low-mass stars with the radial velocity method is hampered by the fact that these stars are very faint at optical wavelengths where the most high-precision spectrometers operate. We investigate the precision that can be achieved in radial velocity measurements of low mass stars in the near infrared (nIR) *Y*-, *J*-, and *H*-bands, and we compare it to the precision achievable in the optical assuming comparable telescope and instrument efficiencies. For early-M stars, radial velocity measurements in the nIR offer no or only marginal advantage in comparison to optical measurements. Although they emit more flux in the nIR, the richness of spectral features in the optical outweighs the flux difference. We find that nIR measurement can be as precise than optical measurements in stars of spectral type \sim M4, and from there the nIR gains in precision towards cooler objects. We studied potential calibration strategies in the nIR finding that a stable spectrograph with a ThAr calibration can offer enough wavelength stability for m s^{-1} precision. Furthermore, we simulate the wavelength-dependent influence of activity (cool spots) on radial velocity measurements from optical to nIR wavelengths. Our spot simulations reveal that the radial velocity jitter does not decrease as dramatically towards longer wavelengths as often thought. The jitter strongly depends on the details of the spots, i.e., on spot temperature and the spectral appearance of the spot. At low temperature contrast (\sim 200 K), the jitter shows a decrease towards the nIR up to a factor of ten, but it decreases substantially less for larger temperature contrasts. Forthcoming nIR spectrographs will allow the search for planets with a particular advantage in mid- and late-M stars. Activity will remain an issue, but simultaneous observations at optical and nIR wavelengths can provide strong constraints on spot properties in active stars.

Subject headings: stars: activity — stars: low-mass, brown dwarfs — stars: spots — techniques: radial velocities

1. INTRODUCTION

The search for extrasolar planets with the radial velocity technique has led to close to 400 discoveries of planets around cool stars of spectral type F–M⁵. Fourteen years after the seminal discovery of 51 Peg b by Mayor & Queloz (1995), the radial velocity technique is still the most important technique to discover planetary systems, and radial velocity measurements are required to confirm planetary candidates found by photometric surveys including the satellite missions CoRoT and *Kepler*.

The largest number of planets found around solar-type stars are approximately as massive as Jupiter, and are orbiting their parent star at around 1 AU or below. In order to find Earth-mass planets in orbit around a star, the radial velocity technique either has to achieve a precision on the order of 0.1 m s^{-1} , or one has to search around less massive stars, which would show a larger effect due to the gravitational influence of a companion. Therefore, low-mass M dwarfs are a natural target for the search for low-mass planets with the radial velocity technique. In addition, there seems to be no general argument against the possibility of life on planets that are

in close orbit around an M dwarf (inside the habitable zone; Tarter et al. 2007). So these stars are becoming primary targets for the search for habitable planets.

So far, only a dozen M dwarfs are known to harbor one or more planets (e.g., Marcy et al. 1998; Udry et al. 2007). The problem with the detection of radial velocity variations in M dwarfs is that although they make up more than 70% of the Galaxy including our nearest neighbors, they are also intrinsically so faint that the required data quality can not usually be obtained in a reasonable amount time, at least not in the spectral range most high resolution spectrographs operate at. M dwarfs have effective temperatures of 4000 K or less, and they emit the bulk of their spectral energy at wavelengths redward of $1 \mu\text{m}$. The flux emitted by an M5 dwarf at a wavelength of 600 nm is about a factor of 3.5 lower than the flux emitted at 1000 nm. Thus, infrared spectroscopy can be expected to be much more efficient in measuring radial velocities of low-mass stars.

A second limit on the achievable precision of radial velocity measurements is the presence of apparent radial velocity variations by corotating features and temporal variations of the stellar surface. Such features may influence the line profiles, and that can introduce a high noise level or be misinterpreted as radial velocity variations due to the presence of a planet. Flares on active M dwarfs might not pose a substantial problem to radial velocity measurements (Reiners 2009), but corotating spots probably do. Desert et al. (2007) modeled the effect of a cool spot for observations of sun-like stars at optical wavelengths. Their results hint at a decrease of

¹ Institut für Astrophysik, Georg-August-Universität, Friedrich-Hund-Platz 1, 37077 Göttingen, Germany, Ansgar.Reiners@phys.uni-goettingen.de

² Hamburger Sternwarte, Gojenbergsweg 112, 21029 Hamburg, Germany

³ Emmy Noether Fellow

⁴ Marie Curie International Incoming Fellow

⁵ <http://www.exoplanet.eu>

spot-induced radial velocity signals towards longer wavelengths. Martín et al. (2006) report the decrease of a radial velocity signal induced by a starspot on the very active M9 dwarf LP 944-20 ($v \sin i \approx 30 \text{ km s}^{-1}$); the amplitude they find is 3.5 km s^{-1} at optical wavelengths but only an rms dispersion of 0.36 km s^{-1} at $1.2 \mu\text{m}$. Thus, observations at infrared wavelength regions may substantially reduce the effect of stellar activity on radial velocity measurements, which would allow the detection of low-mass planets around active stars.

In this paper, we investigate the precision that can be reached in radial velocity measurements at infrared wavelength regions. The first goal of our work is to study the detectability of planets around low-mass stars using infrared spectrographs. We focus on the wavelength bands Y , J , and H because these are the regions where spectrographs can be built at relatively low cost. Extending the wavelength coverage to the K -band imposes much larger costs because of severe cooling requirements and large gaps in the spectral format. We chose to exclude this case from the current paper. Our second motivation is to see to what extent the radial velocity signal of active regions can be expected to vanish at infrared wavelength regions. So far, only rough estimates based on contrast arguments are available, and no detailed simulation has been performed.

The paper is organized as follows. In §2, we introduce the spectral characteristics of M dwarfs and compare model spectra used for our simulations to observations. In §3, we calculate radial velocity precisions that can be achieved at different wavelengths, and we investigate the influence of calibration methods. In §4, we simulate the effect of starspots on radial velocities in the infrared, and §5 summarizes our results.

2. NEAR INFRARED SPECTRA OF M DWARFS

M dwarfs emit the bulk of their flux at near-infrared (nIR) wavelengths between 1 and $2 \mu\text{m}$. However, high-resolution spectrographs operating in the nIR are not as ubiquitous as their counterparts in the optical. Therefore, our knowledge about M dwarf spectra past $1 \mu\text{m}$ is far behind what is known about the visual wavelength range. Another complication is that strong absorption bands of water from the Earth’s atmosphere cover large fractions of the nIR wavelength range. Only some discrete portions of the region $1 - 2 \mu\text{m}$ can be used for detailed spectroscopic work. For our investigation of radial velocity precision in M dwarfs, we concentrate on the three bands, Y , J , and H between the major water absorption bands.

We show in Fig. 1 the transmission spectrum of the Earth’s atmosphere together with band identification that we use in the following. We modeled the telluric features using the FASCODE algorithm (Clough et al. 1981, 1992), a line-by-line radiative transfer code for the Earth’s atmosphere, and HITRAN (Rothman et al. 2005) as a database for molecular transitions. Our model is based on a MIPAS⁶ *nighttime* model atmosphere with updated temperature, pressure and water vapor profiles for the troposphere and lower stratosphere based on GDAS⁷ meteorological models for Cerro Paranal (see

Seifahrt et al. submitted to A&A). Fig. 1 shows that the wavelength regions between Y , J , and H are not useful for spectroscopic analysis of stars. Furthermore, it is important to note that the bands themselves are not entirely free of telluric absorption lines. While the Y -band shows relatively little telluric contamination, the J - and H -bands have regions of significant telluric absorption that must be taken into account when radial velocities are measured at these wavelengths. In our calculations, we mask out the regions that are affected by significant telluric absorption (see §3.1).

Observed low-resolution ($R \approx 2000$) infrared spectra of cool stars and brown dwarfs were presented by McLean et al. (2003) and Cushing et al. (2005). High-resolution infrared spectra of M dwarfs are still very rare; McLean et al. (2007) and Zapatero-Osorio et al. (2007) show J -band spectra of M, L, and T dwarfs taken with NIRSPEC at $R \approx 20,000$. Hinkle et al. (2003) report measurements of rotational velocities from short portions of $R \approx 50,000$ K -band spectra taken with the Phoenix infrared spectrograph, and Wallace & Hinkle (1996) show K -band spectra of cool stars at $R \approx 45,000$. Short H -band spectra of cool stars with a focus on OH lines are presented by O’Neal et al. (2001), in particular they show that OH is present in M dwarfs but weaker than in giants and subgiants.

The high-resolution spectrum that is probably closest to the appearance of an M dwarf spectrum, and that fully covers the wavelength range considered in this paper (Y , J , and H) is the spectrum of a sunspot. Wallace & Livingston (1992) and Wallace et al. (1998) presented spectra of a sunspot in the visual and nIR regions, and in the nIR up to $5.1 \mu\text{m}$, respectively. However, the sunspot spectrum does not resemble the spectra of M dwarfs at high detail, and it cannot be used to investigate a range of temperatures among the M dwarfs. The sunspot spectrum is probably closest to an early-M dwarf with low gravity (Maltby et al. 1986), and we use it below only as a cross-check for the existence of absorption features predicted in our models.

To investigate the radial velocity precision that can be reached using nIR spectra of M dwarfs, we used model spectra calculated with the PHOENIX code (e.g., Hauschildt et al. 1999; Allard et al. 2001). This strategy has the advantage that we can use the full wavelength range without any restrictions imposed by the unavailability of empirical data, and that we can model stars of any temperature and surface gravity. The caveat, however, is that the model spectra may not adequately resemble real stellar spectra, in particular at the high spectral resolution we require.

We show in Fig. 2 three model spectra of cool dwarfs, spectral types are approximately M3, M6, and M9, i.e., effective temperatures of $T = 3500$, 2800 , and 2600 K , respectively. We use models with a surface gravity of $\log g = 4.75$ throughout this paper. The spectra reproduce the data shown by McLean et al. (2003) and Cushing et al. (2005) reasonably well when degraded to low-resolution. In Fig. 3, we show short parts of the model spectra at Y -, J -, and H -bands at higher detail for the case of an M3 star ($T = 3500 \text{ K}$). The three spectral windows in Fig. 3 all cover the same number of resolution elements assuming the spectral resolution is the same in all bands. Obviously, the Y -band is very rich in

⁶ <http://www-atm.physics.ox.ac.uk/RFM/atm/>

⁷ <http://www.arl.noaa.gov/ready/cmet.html>

structure. There are only a few deep lines in the J -band, and the number of sharp features in the H -band is lower than in the Y -band, but higher than in the J -band.

The model shown in Fig. 3 is at the hot end of targets we are interested in. Comparison to Fig. 2 indicates that with lower temperature, the features in the Y -band become stronger. The same is true for features in the J -band, but the H -band becomes relatively featureless at late-M spectral class, which is mainly due to the disappearance of OH lines. In Fig. 3, we also show the sunspot spectrum in comparison to the M3 model spectrum. The FeH lines in the sunspot Y -band are somewhat weaker than in M dwarfs and are strongly affected by Zeeman broadening (Reiners & Basri 2006), the latter leading to significantly reduced depths for many lines in the sunspot spectrum. In the J - and the H -bands, the main features and their depth are relatively well described, so that our model spectra likely reproduce the stellar spectrum relatively well, at least at this temperature.

Another comparison of our models to an observed high-resolution spectrum of a mid-M dwarf is shown in Fig. 4, where we compare an observed spectrum of GJ 1002 (M5.5) to a model spectrum at a temperature of 3200 K. The observed spectrum was obtained by us using CRIRES (Käufl et al. 2006) at the Very Large Telescope (VLT) and reduced following standard infrared reduction procedures including bias- and sky-subtraction, flatfielding, and wavelength calibration using ThAr lines. The model lines (predominantly from FeH) provide a good fit to the observed spectrum of GJ 1002. Thus, we feel confident that our model spectra reproduce the FeH band in the Y -band in M dwarfs reasonably well. More generally, all these comparisons suggest that the PHOENIX model spectra are accurate enough for simulations of radial velocities measured from the nIR spectra of M dwarfs.

3. RADIAL VELOCITY PRECISION

3.1. Calculation of radial velocity precision

The achievable precision of a radial velocity measurement from a spectrum of given quality was calculated by Connes (1985) and Butler et al. (1996). This value is a general limit for radial velocity measurements; it reflects the limited intrinsic information content of any observed spectrum. For example, if a star exhibits more lines in a certain wavelength range, this will lead to a higher precision compared to a star with fewer lines. Similarly, a set of shallow, perhaps blended, lines will put a weaker constraint on the radial velocity than a set of narrow, deep lines. In their Eq. 6, Butler et al. (1996) provide a formula for the radial velocity uncertainty as a function of intrinsic content, instrument resolution (R), and signal-to-noise ratio (S/N). This value is inversely proportional to the weighted sum of the spectrum derivative, which means that the precision is higher as the spectrum has more deep and sharp features. In the following, we first calculate the intrinsic radial velocity precision achievable in a stellar spectrum at given R and S/N . In a second step, we ask how this precision is affected by the limited precision of the wavelength calibration (§3.3).

In order to compare the potential of different wavelength bands, we take a model spectrum, assume a S/N at one given wavelength, and calculate the S/N at other wavelengths according to the spectral flux distribution.

We assume constant instrument efficiency at all wavelengths, and let the signal quality vary according to the stellar flux distribution. We also assume constant spectral resolution and sampling at different wavelength ranges. Calculating the S/N from the spectral flux distribution, it is important to use the number of photons per spectral bin instead of energy per spectral bin, which is provided by the PHOENIX model spectra. To convert energy flux into photon flux, we need to divide by the energy carried per photon, which is hc/λ . Neglecting the constants, this means we need to multiply the spectrum with λ .

For our calculations, we assume an average S/N of 100 at a resolving power of $R = 60,000$ in the Y -band. To account for the spectral resolution, we apply an artificial broadening to the spectra so that the lines become wider, and we assume that the instrument collects a constant number of photons per wavelength interval, i.e., more photons are available per bin at lower spectral resolution. Note that this approach ignores the possibly higher losses from using a narrower slit or other design differences to achieve higher resolution that are likely in practice. That is, a real spectrograph would likely deliver more photons per wavelength interval when used in a lower resolution mode. As this effect is likely a lower-order consideration than the effect of varying dispersion, and is also difficult to predict in a general sense, we do not consider it here.

3.2. Impact of telluric lines

Near infrared wavelength regions are more severely affected by telluric contamination than the optical range. The limiting effect of telluric contamination lies in the difficulty removing it to a level at which it does not affect the radial velocity measurement on a m s^{-1} level. For example, Bean et al. (2009) report a limit of 5 m s^{-1} that can be reached when spectral regions with telluric lines are included in the analysis. To reach higher precision, contaminated regions need to be excluded from the analysis.

In our calculations, we mask the regions affected by telluric lines and do not use them for our analysis of radial velocity precision. We chose to ignore all spectral regions that fall in the vicinity of $\pm 30 \text{ km s}^{-1}$ around a telluric absorption of 2% or more, which is approximately the span introduced by maximum barycentric velocity differences. The telluric transmission spectrum was artificially broadened to a spectral resolving power of $R = 100,000$ before the 2% cutoff was applied. The exact regions that fulfill this criterion also depend on the atmospheric conditions. The wavelength bands together with the fractions ignored due to contamination with telluric lines are summarized in Table 1. The telluric contamination in the V -band is rather small (2%), and does not badly affect the Y -band either ($< 20\%$). On the other hand, roughly half of the spectrum in the J - and H -bands (55% and 46%, respectively) is affected by telluric contamination. The effect on the theoretical information content of the stellar spectrum hence is $\sim \sqrt{2}$, which is still not an order-of-magnitude effect but can no longer be neglected. At these wavelengths, one has to decide whether the RV precision is higher after discarding the contaminated spectral range, or if one should attempt to correct for the telluric contamination.

We note that the same exercise for the K -band (2050–

TABLE 1
WAVELENGTH COVERAGE OF THE SPECTRAL WINDOWS USED IN THIS WORK AND THE FRACTION OF THE WAVELENGTH RANGE AFFECTED BY TELLURIC CONTAMINATION.

Band	V	Y	J	H
λ -range [nm]	505–595	980–1110	1200–1330	1510–1735
telluric loss	2 %	19 %	55 %	46 %

2400 nm) shows that about 80 % of this wavelength range is affected by significant telluric contamination. Clearly, radial velocity work in the *K*-band faces very severe limitations due to telluric lines.

3.3. Wavelength calibration methods

A critical part of radial velocity measurements is the wavelength calibration. When considering such measurements in new spectral regimes the influence of available calibration precision must be considered in addition to the intrinsic information content of the spectra of the stars of interest. There are generally two types of wavelength standards that are being used very successfully at optical wavelengths for high-precision radial velocity work; 1) the calibration signal is injected in the spectrograph following a separate path, e.g., using a ThAr emission lamp (Pepe et al. 2002), and 2) the calibration signal is imposed on the stellar light using a gas absorption cell (e.g. I₂, Butler et al. 1996). At nIR wavelengths, both techniques so far have not been used at the same level of efficiency as in the optical, mainly because no instruments are yet available that can provide comparable spectral resolving power and wavelength range as instruments operating at optical wavelengths. However, such spectrographs are foreseen for the future, and we estimate the precision of both techniques and their current applicability in the nIR. We cast these calculations in terms of equivalent radial velocity precision so that they may be compared directly to the estimated information content of the stellar spectra. For our purpose, we have not considered calibration using a laser comb (Steinmetz et al. 2008) or an etalon, which essentially follow the same principle as the ThAr calibration. A laser comb or etalon that cover the full desired wavelength range would largely solve the problems of inadequate wavelength coverage. Unfortunately, both are not yet available and we restrict the discussion to the ThAr and gas cell options.

3.3.1. ThAr lamp

In the nIR, the ThAr method could in principle just be copied from the optical regime. Standard ThAr lamps produce fewer lines in the nIR, but that does not necessarily mean that the precision over large wavelength regions must be lower than at optical wavelengths. For example, Kerber et al. (2008) provide a list of ThAr lines that includes more than 2400 lines in the range 900 – 4500 nm. Lovis et al. (2006) found that the Ar lines produced by a ThAr lamp are unsuitable for high precision wavelength calibration because they show high intrinsic variability on the order of tens of m s^{-1} between different lamps. Nevertheless, Kerber et al. (2008) show that in the wavelength range we consider here, the fraction of Ar lines in the ThAr lamp spectrum is only on the

order of $\sim 15\%$, and these authors also discuss that the pressure sensitivity only appears in the high-excitation lines of Ar I. So although there are fewer lines than in the optical, the still high number of possible lines suggests that a ThAr lamp should be evaluated as a possible wavelength calibration.

To estimate the calibration precision that can be reached with a ThAr spectrum in a given wavelength interval, we count the number of lines contained in this interval in the list of Kerber et al. (2008), and we estimate the uncertainty in determining the position of every line (converted to radial velocity units) according to its intensity. We assume that we only take one exposure of the ThAr lamp, and we scale the line intensities to a given dynamic range. The range ultimately used for our calculations was selected to achieve a high number of useful lines while losing as few lines as possible due to detector saturation. We quadratically add the uncertainties of all lines to calculate the total uncertainty of a ThAr calibration at the chosen spectral region. “Saturated” lines are not taken into account, but we note that infrared detectors offer advantages over CCDs in this regard. One advantage of infrared detectors is that saturated pixels do not bleed into neighboring pixels like in CCDs. Therefore, although a particular calibration line may saturate some pixels, the problem would be localized only to the pixels the line falls on and the signals recorded for lines falling on neighboring pixels would be unaffected. In practice then, some lines may be allowed to saturate and thus be ignored during the wavelength calibration if a higher overall signal would result in a net gain of useful lines. A second issue is that individual pixels in infrared detectors can be read out at different rates. Therefore, there is the possibility of an increased dynamic range for a given exposure level. However, it is unclear what would be the influence of the differences in response and noise properties that pixels read out at different rates would have. So for this work we take the conservative approach that lines which would apparently saturate given our selected dynamic range can not be used for the wavelength calibration.

Our estimation of the utility of a ThAr lamp for wavelength calibration in order to obtain high-precision radial velocities is based on the assumption that the calibration is only needed to track minor changes in the instrument response. Such is true for an isolated and stabilized instrument with a nearly constant pupil illumination (e.g. like HARPS, Mayor et al. 2003). The main reason is that the light from a ThAr lamp will not pass directly through the instrument in the exact same way and/or at the exact same time as the light from a star. Therefore, the utility of ThAr as a calibration for radial velocity measurements will be reduced from that discussed here for instruments that experience significant temporal variations.

3.3.2. Gas absorption cell

The gas absorption technique requires a gas that provides a large number of sharp spectral lines. Currently, no gas has been identified that produces lines in the full nIR wavelength range at a density comparable to I₂ spectrum in the optical (I₂ only provides lines in the optical wavelength range), although there have been some investigations into gases suitable for small windows in this region. D’Amato et al. (2008) report on a gas absorp-

tion cell using halogen-hydrates, HCl, HBr, and HI, that has absorption lines between 1 and $2.4\ \mu\text{m}$, but these gases only produce very few lines so that a calibration of the wavelength solution and the instrumental profile can only be done over a small fraction of the spectrum. Mahadevan & Ge (2009) discuss various options for nIR gas cells and conclude that the gases $\text{H}^{13}\text{C}^{14}\text{N}$, $^{12}\text{C}_2\text{H}_2$, ^{12}CO , and ^{13}CO together could provide useful calibration in the H -band. Another gas that provides some utility in the nIR is ammonia (NH_3), which exhibits a dense forest of spectral lines in the K -band. We are currently using an ammonia cell for a radial velocity planet search with CRILES at the VLT. More details about the cell and these radial velocity measurements are contained in another paper (Bean et al. 2009).

For an estimate of the calibration precision that could potentially be achieved over a broad wavelength range using a gas cell, we assume that a gas or combination of gases might be found with absorption lines similar to ammonia, but throughout the entire nIR region. We calculate the radial velocity precision from a section of an ammonia cell spectrum with various S/N and R just as for the stellar spectra (i.e. using Eq. 6 in Butler et al. 1996). The basis for this calculation is a 50 nm section of a spectrum of our CRILES ammonia cell (18 cm length and filled with 50 mb of ammonia) measured with an FTS at extremely high-resolution ($R \sim 700,000$). Convolved to a resolving power of $R = 100,000$ and $S/N = 100$, the calculated precision is $9\ \text{m s}^{-1}$. We note that this value would change if a longer cell or higher gas pressure would be used, but this change would be relatively small for conceivable cells. To extrapolate the precision estimate to arbitrary wavelength regions we scale the calculated value by the corresponding size of the regions. For example, the uncertainty from a region of 100 nm would be a factor of $\sqrt{2}$ less than that calculated for the 50 nm region.

We emphasize that our estimates on the performance of a gas cell in the nIR are purely hypothetical. Currently, in the wavelength range under consideration, we know of no real gas that shows as dense a forest of lines in the Y -, J -, and H -bands as ammonia does in the K -band.

3.4. Radial velocity precision in low-mass stars

The precision that can be achieved using (model) spectra of stars at 3500 K (M3), 2800 K (M6), and 2400 K (M9) for different wavelength regions are summarized in Table 2 and shown in Fig. 5. For each case, we first calculated the intrinsic precision over the wavelength bin under consideration. As explained in §3, we assume S/N of 100 at $1\ \mu\text{m}$ at $R = 60,000$ and scale the signal quality according to the spectral flux distribution and spectral resolution. The differences between radial velocity precisions at different wavelength bands are dominated by the differences between the S/N and between the appearance of spectral features in these bands (see Figs. 2 and 3). A secondary effect is the length of the spectral range that differs between the bands, but it is not always the band with the largest coverage that yields the highest precision. We show the situation for three different values of $R = 100,000, 80,000,$ and $60,000$.

The S/N given in Table 2 varies according to the number of photons per pixel, which decreases at higher spec-

TABLE 2
WAVELENGTH-DEPENDENT S/N AND RADIAL VELOCITY PRECISION THAT CAN BE ACHIEVED FROM DATA OF THIS QUALITY. THE UPPER PART OF THE TABLE SHOWS THE RESULTS FOR AN M3 STAR, THE MIDDLE FOR AN M6, AND THE LOWER PART FOR AN M9 STAR.

Resolution	S/N				RV precision [m s^{-1}]			
	V	Y	J	H	V	Y	J	H
Spectral Type M3								
60000	50	100	101	95	3.6	5.7	22.9	10.0
80000	43	86	87	82	2.9	4.4	18.1	8.4
100000	39	77	78	74	2.5	3.8	15.5	7.6
Spectral Type M6								
60000	20	100	114	107	4.7	3.8	11.2	9.7
80000	18	86	99	93	3.7	3.0	8.8	7.8
100000	16	77	88	83	3.2	2.6	7.5	6.9
Spectral Type M9								
60000	12	100	134	128	8.0	2.2	4.6	4.0
80000	10	86	116	111	6.2	1.7	3.5	3.5
100000	9	77	104	99	5.3	1.5	2.9	3.3

tral resolution because the wavelength bins per pixel become smaller. The S/N is always comparable between the three nIR bands, but the optical wavelength range provides S/N that is about a factor of two smaller in the M3, a factor of five smaller at M6, and a factor of ten smaller in the M9 star.

In addition to the intrinsic precision, we show the precision achievable if an imperfect wavelength calibration is considered. The additional uncertainty due to ThAr or gas cell calibration (see §3.3) leads to somewhat higher limits that can be achieved in a real observation. We show no ThAr or gas cell values for the V -band because here the wavelength calibration is not the critical factor for the situations investigated in this paper.

The question Fig. 5 tries to answer is what is the highest attainable precision of a radial velocity measurement if a given star is observed at different wavelength regions and spectral resolutions, under the assumption of the same exposure time, telescope size, and instrument throughput for all setups.

For an early-M star (M3), the highest precision is still reached in the V -band, although the Y -band does not perform much worse. For the given choice of parameters, the highest obtainable precision in the V -band at $R = 100,000$ is roughly $2.5\ \text{m s}^{-1}$, and in the Y -band it is $\sim 3.8\ \text{m s}^{-1}$. The J - and H -bands are worse with only $\sim 16\ \text{m s}^{-1}$ and $8\ \text{m s}^{-1}$ precision, respectively, at the highest resolution. In general, in the absence of rotation, higher precision is obtained for higher spectral resolving power⁸. We discuss the limits to the precision in rotating stars in §3.5. A remarkable feature of our precision calculations for $T = 3500\ \text{K}$ is that although the flux level in the visual wavelength range is much lower than the flux around $1\ \mu\text{m}$ and redder, the radial velocity precision is not worse. This is because the optical spectrum of an early-M dwarf is extremely rich in narrow

⁸ As an approximation, precision scales linearly with S/N but quadratically with R . If a constant number of photons is assumed, S/N scales down with \sqrt{R} , and as a result, the precision scales approximately with $R^{3/2}$.

features. At nIR wavelengths, the number of features is much lower so that the attainable precision is lower, too. The same explanation holds for the comparison between the nIR Y -, J -, and H -bands. The low precision obtainable in the J -band is due to the lack of sharp and deep spectral features in that wavelength range (compare Figs. 2 and 3).

At lower temperature, $T = 2800$ K (M6), the overall precision (at the same S/N , that means in general after longer exposures) has gained in the nIR-bands in comparison to the optical, because now the S/N is much higher at nIR regions. The Y - and J -band precisions improve a lot in comparison to the M3 star, which is also due to the appearance of FeH bands (see Cushing et al. 2005). The H -band precision at 2800 K is comparable to the 3500 K spectrum. Now, the V -band performs worse than the Y -band, but still it yields a remarkably high precision: Although the flux level in the V -band is about an order of magnitude below the flux at nIR wavelengths, the richness in sharp features can almost compensate for this. The V -band precision is only about 30 % worse than the Y -band precision, and it still yields much better precision than the J - and the H -bands.

Finally, in the M9 star at $T = 2400$ K, all three nIR bands outperform the V -band because of the high flux ratio between the nIR and the optical range. Still, the Y -band provides the highest precision about a factor of two better than the J - and the H -band.

We consider now the effects of limited precision in the wavelength calibration using the ThAr lamp or a gas cell (shown in in Fig. 5 as open rhombs and crosses, respectively). The ThAr calibration apparently can provide a very reliable calibration that introduces only a few percent loss in precision. Of course, in a real spectrograph, effects like wavelength stability over time additionally limit the precision that can be reached (Lovis & Pepe 2007). This effect has not been taken into account. Nevertheless, our calculations show that enough suitable ThAr lines are available and that a wavelength solution at nIR wavelengths ($Y - H$ -bands) based on ThAr lines is a reliable calibration that can in principle be expected to work almost as successfully as in the optical wavelength range. In contrast to that, the calibration using the virtual gas cell as a reference yields much worse a result, in particular at short wavelengths like in the Y -band. In order to make the gas-cell calibration provide the same accuracy as a calibration using a ThAr lamp (in a stabilized spectrograph), a gas is needed that provides more and deeper lines than NH_3 provides in the K -band. So far, all gases known provide many fewer lines so that currently achievable precision turns out to be significantly below than what can be achieved with ThAr. We note that in order to make the gas cell calibration work, the spectrum must have a minimum S/N allowing a reliable reconstruction of the instrument profile. This means a typical minimum S/N of ~ 100 is required for the gas cell method. Thus, using a gas cell for the wavelength calibration, low- S/N spectra as in the M6 and M9 cases in the V -band considered above could not be used.

3.5. The influence of rotation

3.5.1. Distribution of rotation in M dwarfs

Higher resolution spectra only offer an advantage for radial velocity measurements if the stars exhibit sharp lines (see also Bouchy et al. 2001). Field mid- and late-M dwarfs can be very rapid rotators with broad and shallow spectral lines. For example, Reiners & Basri (2008) show that rapid rotation is more frequent in cooler M dwarfs. We have collected measurements on rotational velocities from Delfosse et al. (1998); Mohanty & Basri (2003); Reiners & Basri (2008) and Reiners & Basri (submitted to ApJ), and we show the cumulative distributions of $v \sin i$ for early-, mid-, and late-M stars in Fig. 6. All early-M dwarfs (M1 – M3) in the samples are rotating slower than $v \sin i = 7 \text{ km s}^{-1}$, which means that early-M dwarfs are very good targets for high precision radial velocity surveys. Among the mid-M dwarfs (M4 – M6), about 20 % of the stars are rotating faster than $v \sin i = 10 \text{ km s}^{-1}$, and this fraction goes up to about 50 % in the late-M dwarfs (M7 – M9).

3.5.2. Rotational broadening and radial velocity precision

We show in Fig. 7 the Y -band precision of radial velocity measurements that can be achieved in a 3000 K star (M5) as a function of projected rotational velocity at different spectral resolutions ($R = 20,000, 60,000, 80,000,$ and $100,000$). All assumptions about S/N and R are as explained above.

As expected, at high rotation velocities ($v \sin i > 30 \text{ km s}^{-1}$), the precision achieved with spectrographs operating at different R are hardly distinguishable. Only if the line width of the rotating star is narrower than the instrumental profile does higher resolution yield higher precision. However, for $R > 60,000$, the difference in precision is relatively small even at very slow rotation. At a rotation velocity of $v \sin i = 10 \text{ km s}^{-1}$, the precision is roughly a factor of 3 lower than the precision in a star with $v \sin i = 1 \text{ km s}^{-1}$, and $v \sin i = 6 \text{ km s}^{-1}$ brings down the precision by about a factor of 2 compared to $v \sin i = 1 \text{ km s}^{-1}$.

4. RADIAL VELOCITY VARIATIONS FROM STARSPOTS

In this Section, we investigate the influence of starspots on the measurement of radial velocities. A similar study was performed by Desert et al. (2007), but for sun-like stars in the optical wavelength regime. We extend this study to cooler stars and nIR wavelengths.

4.1. Spot properties

Radial velocity variations can be mimicked by surface features corotating with the star. We know from the Sun that magnetic activity can cause spots that are significantly cooler than the photosphere, and much larger spots are found on stars more active than the Sun (in general, rapidly rotating stars are more active). However, the temperature differences between starspots and the corresponding “quiet” photosphere remains a rather unknown parameter, especially for very active stars.

The coolest temperatures in large sunspots can be ~ 2000 K lower than the temperature in the surrounding photosphere (Solanki 2003). Observed as a star, however, such differences would still be difficult to observe because sunspots cover only a very small fraction of the surface

(< 1%). O’Neal et al. (2001, 2004) reported spot temperatures up to 1500 K below photospheric temperatures in active G- and K-type stars. These spots cover between 10 and 50 % of the stellar surface. Strassmeier & Rice (1998) reported spot temperatures in an active K dwarf that are ~ 800 K below the effective photospheric temperature based on Doppler imaging.

From the available observations, no general prediction on the occurrence and properties of spots on stellar surfaces is possible. In particular, no observational information is available on spot distributions on M dwarfs, which have atmospheres significantly different than those of sun-like stars, and may also have different magnetic field topologies (Donati et al. 2008; Reiners & Basri 2009). Therefore, we investigate a set of different photosphere and spot temperature combinations in the following.

Before we investigate apparent radial velocity shifts using a detailed model (§4.2), we consider a “toy model” of an ideal spectral line composed of signal from two regions: the “quiet” surface of a rotating star, and a co-rotating, cool spot. To demonstrate the influence of the temperature contrast and differing spectral features for a spot, we generate the line profiles sampled over a complete rotational period and compute the apparent radial velocity shift for each rotational phase by fitting them with a Gaussian. An example radial velocity curve is given in Fig. 8. We report on the amplitude K of the radial velocity curve occurring during a full rotation⁹.

4.1.1. Contrast

One crucial parameter for the influence of a starspot on a spectral line, and thus the star’s measured radial velocity, is the flux contrast between the quiet surface and the spot at the wavelength of interest. In general, one expects the radial velocity amplitude due to a spot to be smaller with lower contrast and vice versa. We illustrate the effect of a cool spot on the line profile and the measured radial velocity shift in Fig. 9, where the situation for a spot covering 2 % of the visible surface is shown for two different temperatures (contrasts).

To investigate the influence of contrast over a wide range of parameters we used the toy model described above. We assumed a blackbody surface brightness according to a surface temperature T_0 , and we subtracted the amount of flux that originates in a spot covering 2 % of the stellar surface. We then added the flux originating in the spot at a temperature T_1 . This spot has the same line profile as the photosphere, which means that we assume a constant line profile for the whole star. For our example, we chose a rotational velocity of $v \sin i = 2 \text{ km s}^{-1}$.

In Fig. 10, we show the wavelength-dependent flux ratio between the quiet photosphere and the spot (the contrast, upper panel), and the resulting apparent radial velocity shift from the toy model calculations (lower panel). We show cases for three photosphere temperatures T_0 (5700 K, 3700 K, and 2800 K), for each T_0 we show cases with a small temperature difference, $T_0 - T_1 = 200$ K, and with a larger temperature difference of $(T_0 - T_1)/T_0 = 0.35$.

For small temperature differences (left panel of

Fig. 10), the flux ratio between photosphere and spot decreases by approximately a factor of two in the range 500 – 1800 nm, while the radial velocity (RV) signal decreases by roughly a factor between two and three. The RV signal is higher for the lowest T_0 because the relative difference between T_1 and T_0 is much larger than in the case of $T_0 = 5700$ K.

The cases of large temperature contrast (right panel in Fig. 10) produce flux ratios > 100 in the coolest star at 500 nm. At 1800 nm the flux ratio decreases to a value around 5, i.e., a factor of 20 lower than at 500 nm. This is much larger than for the cases with small temperature contrast, where the flux ratio only decreases by a factor of two or less. On the other hand, the RV signal does not change as dramatically as the flux ratio. For large temperature contrasts, the absolute values of the RV signal are larger than in the case of low contrast, but the slope of RV with wavelength is much shallower; it is well below a factor of two in all three modeled stars. The explanation for this is that the large contrast in flux ratio implies that the spot does not contribute a significant amount to the full spectrum of the star at any of these wavelengths. Therefore, a relatively small change of the flux ratio with wavelength has no substantial effect on the RV signal. If, on the other hand, the flux ratio is on the order of two or less, a small decrease in the ratio with wavelength means that the larger contribution from the spot can substantially change the RV signal. Thus, a significant wavelength dependence for an RV signal induced by a cool spot can only be expected if the temperature difference between the quiet photosphere and the spot is not too large.

4.1.2. Line profile in the spot

Line profile deviations that cause radial velocity variations do not solely depend on temperature contrast but also on the dependence of spectral features on temperature; effective temperature generally corresponds to a different spectrum and does not just introduce a scaling factor in the emitted flux. For example, a spectral line variation, and hence a radial velocity shift, can also appear at zero temperature contrast if the spectral line depths differ between the spot and the photosphere (as for example in hot stars with abundance spots; Piskunov & Rice 1993).

In Fig. 11, we consider a similar situation as in Fig. 9. Here, the temperature contrast between spot and photosphere is held constant but we show three cases in which the depths of the spectral line originating in the spot are different. The three spot profiles are chosen so that the line depths are 0.5, 1.0, and 1.5 times the line depth of the photospheric line. Fig. 11 illustrates that if spectral features are weaker in the spot than in the surrounding photosphere, the radial velocity shift (bottom panel) is larger than in the case of identical line strengths. If, on the other hand, the spectral features become stronger, as for example in some molecular absorption bands, the spot signature weakens and the radial velocity distortion is smaller. In our example of a stronger spot feature, this effect entirely cancels out the effect of the temperature contrast, so that the radial velocity signal of the spot is zero although a cool spot is present.

4.2. Spot simulations

⁹ Desort et al. (2007) report peak-to-peak amplitude, which is twice the value we are using.

After considering the general effects of starspots in the last Section, we now discuss results of a more sophisticated simulation. Here, we calculate a full spectrum by integrating over the surface of a spotted star using spectra from a model-atmosphere code. The resulting radial velocity shift is estimated by cross-correlation against a spectrum unaffected by spots.

4.2.1. Line profile integration

Our model spectra for a spotted star were calculated using a discrete surface with 500×500 elements in longitude and latitude arranged to cover the same fraction of the surface each. All surface elements are characterized by a ‘local’ temperature; unspotted areas are assigned to the photospheric temperature, and spotted areas contribute spectra pertaining to atmospheres with lower temperatures. The associated spectra $f(\lambda, T)$ were generated with PHOENIX for all temperatures used. Depending on the rotational phase p , the visibility A_i of each surface element i is calculated, considering projection effects. We determine the radial velocity shift $v_{\text{rad},i}$ for each surface element due to the stellar rotation. The resulting model spectrum $f_p(\lambda)$ for the spotted star is

$$f_p(\lambda) = \frac{\sum_{i=1}^N f(\lambda, T_i, v_{\text{rad},i}) A_i}{\sum_{i=1}^N A_i}, \quad (1)$$

where N is the total number of elements.

In all of our calculations the model star has an inclination of $i = 90^\circ$, and for simplicity we assume a linear limb darkening coefficient $\epsilon = 0$ (no limb darkening). Using no limb darkening slightly overestimates the radial velocity signal but captures the qualitative behaviour that we are interested in. Stellar spots are considered to be circular and located at 0° longitude and $+30^\circ$ latitude.

We calculated the RV signal introduced by a temperature-spot on a rotating star. We chose the same star/spot temperature pairs as in the contrast calculations in the foregoing Section, but we used detailed atmosphere models and PHOENIX spectra to calculate the RV signal over the wavelength area 500 – 1800 nm. That means, our calculations include the effects of both the contrast *and* differences in the spectral features between atmospheres of different temperatures.

4.2.2. Results from spot simulations

The results of our calculations are shown in Fig. 12. As in Fig. 10, we show six different stars, the temperature combinations are identical. The spot size is 1% of the projected surface. We compute RV amplitudes for 50 nm wide sections. For each model star, we show four cases for rotational velocities of $v \sin i = 2, 5, 10,$ and 30 km s^{-1} .

In general, the trends seen in the detailed model are consistent with our results from the toy model of a single line taking into account only the flux ratio between photosphere and spot. As long as the flux ratio is relatively small (200 K, left panel in Fig. 12), the RV amplitude strongly depends on wavelength due to the wavelength dependency of the contrast. The strongest gradient in RV amplitude occurs between 500 and 800 nm; the RV

signal decreases by almost a factor of 10 in the lowest temperature model where the flux gradient is particularly steep over this wavelength range. The decrease occurs at somewhat longer wavelengths in the cooler model stars than in the hotter models. In the model stars with a high flux ratio between photosphere and spot (right panel in Fig. 12), the variation in RV amplitude with wavelength is very small. The very coolest model shows a few regions of very low RV amplitude, but the general decline is not substantial.

The absolute RV signal in a Sun-like star with $T_0 = 5700 \text{ K}$ at 500 nm comes out to be $\sim 40 \text{ m s}^{-1}$ at a spot temperature of $T_1 = 3700 \text{ K}$ on a star rotating at $v \sin i = 5 \text{ km s}^{-1}$. This is consistent with the result of Desort et al. (2007), who reported a peak-to-peak amplitude of $\sim 100 \text{ m s}^{-1}$, i.e., an ‘amplitude’ of 50 m s^{-1} , in a similar star. Over the wavelength range they investigated (roughly 500 – 600 nm), Desort et al. found that the RV amplitude decreases by about 10%. We have not calculated the RV amplitude over bins as small as the bins in their work and our calculation only has two bins in this narrow wavelength range. However, we find that the decrease Desort et al. (2007) reported between 500 nm and 600 nm, is not continued towards longer wavelengths. In our calculations, the RV amplitude does not decrease by more than $\sim 20\%$ between 500 and 1800 nm. Similar results apply for higher rotation velocities and lower photosphere temperatures.

The models with lower flux ratio, $T_0 - T_1 = 200 \text{ K}$, show more of an effect with wavelength, although the absolute RV signal is of course smaller. The RV amplitude in a star with $T_0 = 3700 \text{ K}$, a spot temperature of $T_1 = 3500 \text{ K}$, and $v \sin i = 5 \text{ km s}^{-1}$ is slightly above 10 m s^{-1} at 500 nm and $\sim 4 \text{ m s}^{-1}$ at 1000 nm. Above 1000 nm, no further decrease in RV amplitude is observed. The behavior, again, is similar in other stars with low flux ratios and with different rotation velocities.

For the cool models with large temperature differences, the individual RV amplitudes show relatively large scatter between individual wavelength bins. We attribute this to the presence of absorption features in some areas, while other areas are relatively free of absorption features. The temperature dependence of the depth of an absorption feature is important for the behavior of the spot signature in the spectral line. An example of this effect can be observed around 1100 nm, where the spectrum is dominated by absorption of molecular FeH that becomes stronger with lower temperature.

4.2.3. Comparison to LP 944-20

We can compare our simulations to the optical and nIR radial velocity measurements in LP 944-20 reported by Martín et al. (2006). At optical wavelengths, they found a periodical radial velocity variation of $K = 3.5 \text{ km s}^{-1}$, while in the nIR they could not find any periodical variation and report an rms of 0.36 km s^{-1} . The approximate effective temperature of an M9 dwarf like LP 944-20 is around 2400 K, we compare it to our coolest model that has a temperature of $T_0 = 2800 \text{ K}$. The radial velocity amplitude of 3.5 km s^{-1} at visual wavelengths is much higher than the results of our simulations, but this can probably be accounted for by the different size of the

surface inhomogeneities (only 1% in the simulations)¹⁰.

The observations of Martín et al. (2006) suggest a ratio between optical and nIR radial velocity variations larger than a factor of 10. The largest ratio in our set of simulations in fact is on that order; the radial velocity jitter in our model with $T_0 = 2800$ K and $T_1 = 2600$ K diminishes by about a factor of ten between 600 nm and 1200 nm. Extrapolating from the results of the hotter models, in which the ratio between visual and nIR jitter is smaller, we cannot exclude that this ratio may become even larger in cooler stars. Our model with larger temperature contrast ($T_0 = 2800$ K, $T_1 = 1800$ K) produces a smaller ratio between visual and nIR jitter. Thus, our simulations are not in contradiction to the results reported by Martín et al. (2006). A ratio of ten or more in jitter between optical and nIR measurements seems possible if the temperature contrast is fairly small (100–200 K).

We note that no radial velocity variations were actually detected in LP 944-20 in the nIR, which means that at the time of the nIR observations, it simply could have experienced a phase of lower activity and reduced spot coverage. In order to confirm the effects of a wavelength-dependent contrast on radial velocity measurements, observations carried out simultaneously at visual and nIR wavelengths are required.

Martín et al. (2006) propose that weather effects like variable cloud coverage may be the source for the radial velocity jitter in the visual and for the wavelength-dependent contrast. This would probably mean very small temperature contrast but a strong effect in wavelength regions with spectral features that are particularly sensitive to dust. Our simulations do not predict the wavelength dependence of pure dust clouds, but at this point we see no particular reason why the jitter from purely dust-related clouds should be much stronger in the visual than in the nIR. To model this, a separate simulation would be needed taking into account the effects of dust on the spectra of ultracool dwarfs.

5. SUMMARY AND CONCLUSIONS

We have investigated the possibility of measuring radial velocity variations of low-mass stars at nIR wavelengths (Y, J, H). The spectral flux distribution of red stars favors long wavelengths because higher S/N can be achieved in comparison to optical wavelengths. On the other hand, the spectral information content of the spectra (presence of sharp and strong spectral features) is lower at longer wavelengths, and the efficiency of calibration methods is not well established.

For early M dwarfs, nIR radial velocities do not offer any advantage in terms of photon-limited precision. Indeed, the fact that measurement methods in the optical are much more advanced than those in the nIR means that there is not really any motivation of nIR radial velocities from this perspective. On the other hand, at mid-M spectral type, the achievable precision becomes higher in the nIR around spectral type M4–5; Y -band observations can be expected to achieve a radial velocity precision higher than observations at optical wavelengths. At late-M dwarfs, the Y -band outperforms the

V -band precision by about a factor of 4–5. Observations in the J - and H -bands are a factor of 2–5 worse than the Y -band across the M star spectral types. They are only superior to the V -band observations in very-late-M dwarfs.

Our investigation into the effects of activity on radial velocity measurements showed that a crucial parameter for the wavelength dependence of jitter is the temperature contrast between the spot and the photosphere. If the spot temperature is only a few hundred Kelvin below the photospheric temperature, the induced radial velocity signal is on the order of several ms^{-1} in the optical and becomes weaker towards longer wavelengths. Note that the absolute size of this effect depends on the size of the spot (1% in our simulation) and will grow with larger spot size. High temperature contrast, on the other hand, causes a much larger radial velocity signal that only weakly depends on wavelength. For example, in M stars with spots only ~ 200 K cooler than the photosphere, the jitter at nIR wavelengths is roughly a factor of ten lower than at optical wavelengths, but it is smaller than a factor of two if the temperature contrast is 1000 K or higher. Unfortunately, not much is known about spot temperatures, particularly in low-mass stars, but our results show that simultaneous observations at optical and nIR wavelengths can provide useful constraints on the spot temperatures of active stars.

Another important factor for the effect of active regions on radial velocity measurements are the differences between spectral features appearing in the photosphere and the spots. Conventional estimates usually assume that both are comparable, but given the perhaps relatively large temperature contrasts and the strong temperature dependence of the molecular features, this may not be the case. Thus, large differences in the radial velocity signal between different spectral regions can occur if spectral features of different temperature sensitivity appear.

The radial velocity signal may not vanish as expected at nIR wavelengths, and it seems unlikely that strong radial velocity signals observed at optical wavelengths can vanish in the nIR, particularly in very active stars in which relatively large temperature contrast is expected. The advantage of a nIR spectrograph over an optical spectrograph becomes obvious in the late-M dwarfs. Our results point towards a spectrograph covering the wavelength range 500–1150 nm that captures the region where the RV precision is highest at all M spectral classes, and where the wavelength dependence of jitter shows the largest gradient in order to distinguish between orbital motion and spots. Such a spectrograph should be designed to be very stable and could use a ThAr lamp for calibration. In the future, other calibration strategies might become available (e.g. a laser frequency comb, Steinmetz et al. 2008), but the ThAr method can in principle provide the sensitivity required to detect Earth-mass planets around low mass stars.

We thank Peter H. Hauschildt for promptly providing PHOENIX model spectra. A.R. acknowledges research funding from the DFG as an Emmy Noether fellow, A.R. and A.S. received support from the DFG under RE 1664/4-1. J.B. has received research funding from the European Commissions Seventh Framework Programme

¹⁰ Using our “toy model” we estimate that a spot covering $\sim 10\%$ of the surface can generate a velocity amplitude of a few km s^{-1} .

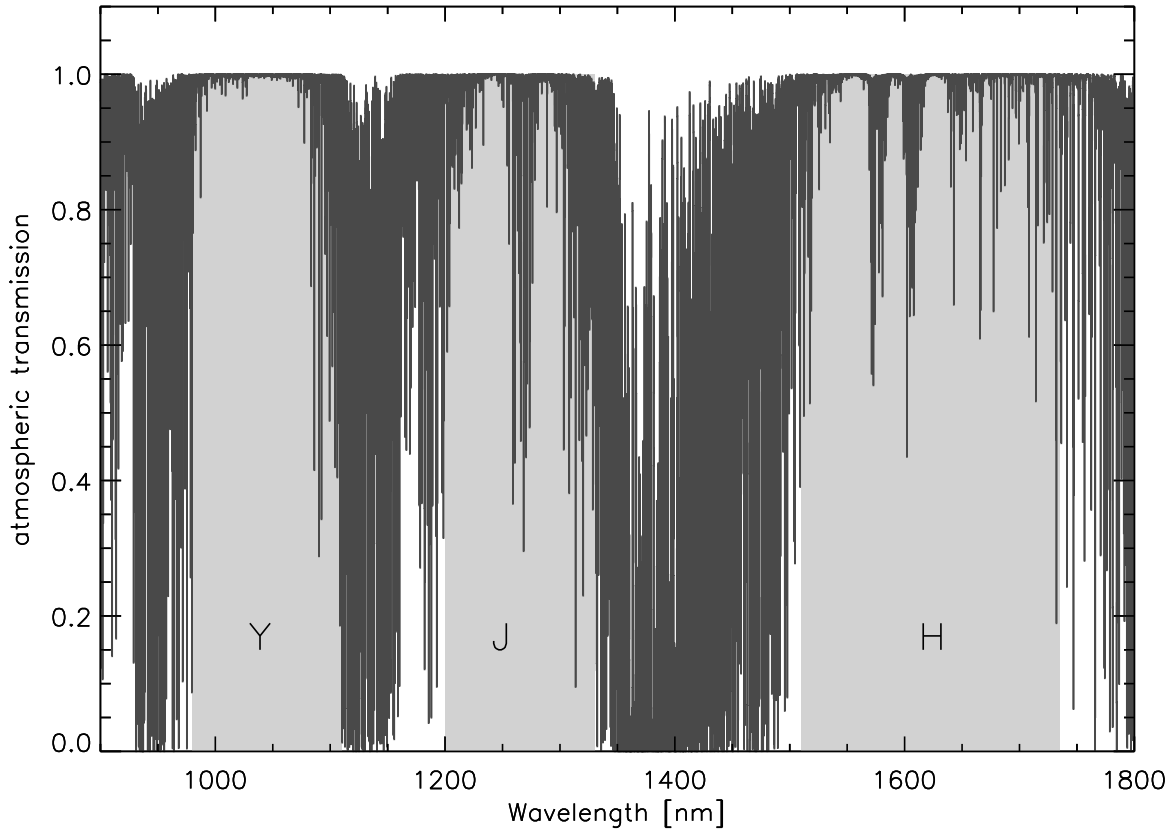


FIG. 1.— Telluric absorption spectrum with the standard windows in the Y -, J -, and H -bands indicated.

as an International Incoming Fellow (PIFF-GA-2009-234866).

REFERENCES

- Allard, F., Hauschildt, P.H., Alexander, D.R., Tamanai, A., & Schweitzer, A., 2001, *ApJ*, 556, 357
- D'Amato, F., et al., 2008, *SPIE*, 7014, 70143V
- Bean, J., Seifahrt, A., Hartmann, H., Nilsson, H., Wiedemann, G., Reiners, A., Dreizler, S., & Henry, T., submitted to *ApJ*, [arXiv:0911.3148](https://arxiv.org/abs/0911.3148)
- Bouchy, F., Pepe, F., & Queloz, D., 2001, *A&A*, 374, 733
- Butler, R.P., Marcy, G.W., Williams, E., McCarthy, C., Dosanji, P., & Vogt, S.S., 1996, *PASP*, 108, 500
- Connes, P., 1985, *Ap&SS*, 110, 211
- Clough, S. A., Kneizys, F. X., Rothman, L. S., & Gallery, W. O. 1981, *Proc. SPIE*, 277, 152
- Clough, S. A., Iacono, M. J., & Moncet, J.-L. 1992, *J. Geophys. Res.*, 97, 15761
- Cushing, M.C., Rayner, J.T., & Vacca, W.D., 2005, *ApJ*, 623, 1115
- Delfosse, X., Forveille, T., Perrier, C., & Mayor, M., 1998, *A&A*, 331, 581
- Desort, M., Lagrange, A.-M., Galland, F., Udry, S., & Mayor, M., 2007, *A&A*, 473, 983
- Donati, J.-F., Morin, J., Petit, P., et al., 2008, *MNRAS*, 390, 545
- Hauschildt, P.H., Allard, F., & Baron, E., 1999, *ApJ*, 512, 377
- Hinkle, K.H., Wallace, L., Valenti, J., & Tsuji, T., 2003, *IAU Symp.* 215, 213
- Käuff, H. U., et al., 2006, *Msngr*, 126, 32
- Kerber, F., Nave, G., & Sansonetti, C. J., 2008, *ApJS*, 178, 374
- Lovis, C., Pepe, F., Bouchy, F., et al., 2006, *Proc. SPIE*, Vol. 6269, 62690P
- Lovis, C., & Pepe, F., 2007, *A&A*, 468, 1115
- Mahadevan, S., & and Ge, J., 2009, *ApJ*, 692, 1590
- Maltby, P., Avrett, E.H., Carlsson, M., Kjeldseth-Moe, O., Kurucz, R.L., & Loeser, R., 1986, *ApJ*, 306, 284
- Marcy, G.W., Butler, R.P., Vogt, S.S., Fischer, D., Lissauer, J.J., 1998, *ApJ*, 505, L147
- Martín, E.L., Guenther, E., Zapatero Osorio, M.R., Bouy, & Wainscoat, R., 2006, *ApJ*, 644, L75
- Mayor, M., & Queloz, D., 1995, *Nature*, 378, 355
- Mayor, M., et al., 2003, *Msngr*, 124, 20
- McLean, I.S., McGovern, M.R., Burgasser, A.J., Kirkpatrick, J.D., Prato, L., & Kim, S.S., 2003, *ApJ*, 596, 561
- McLean, I.S., Prato, L., McGovern, M.R., Burgasser, A.J., Kirkpatrick, J.D., Rice, E.L., & Kim, S.S., 2007, *ApJ*, 658, 1217
- Mohanty, S., & Basri, G., 2003, *ApJ*, 583, 451
- O'Neal, D., Neff, J.E., Saar, S.H., & Mines, J.K., 2001, *AJ*, 122, 1954
- O'Neal, D., Neff, J.E., Saar, S.H., & Cuntz, M., 2004, *AJ*, 128, 1802
- Pepe, F., Mayor, M., Galland, F., Naef, D., Queloz, D., Santos, N.C., Udry, S., & Burnet, M., 2002, *A&A*, 388, 632
- Piskunov, N.E., & Rice, J.B., 1993, *PASP*, 105, 1415
- Reiners, A., 2009, *A&A*, 498, 853
- Reiners, A., & Basri, G., 2006, *ApJ*, 644, 497
- Reiners, A., & Basri, G., 2008, *ApJ*, 684, 1390
- Reiners, A., & Basri, G., 2009, *A&A*, 496, 787
- Reiners, A., & Basri, G., submitted to *ApJ*
- Rothman, L. S., et al. 2005, *Journal of Quantitative Spectroscopy and Radiative Transfer*, 96, 139
- Seifahrt, A., Käuff, H.U., Bean J., Richter, & Siebenmorgen, R., 2010, submitted to *A&A*
- Solanki, S.K., 2003, *A&AR*, 11, 153
- Steinmetz, T., Wilken, T., Araujo-Hauck, C., Holzwarth, R., Hänsch, T. W., Pasquini, L., Manescau, A., & et al. 2008, *Science*, 321, 1335
- Strassmeier, K.G., & Rice, J.B., 1998, *A&A*, 330, 685
- Tarter, J.C., et al., 2007, *Astrobiology*, 7, 30
- Udry, S., Bonfils, X., Delfosse, X., et al., 2007, *A&A*, 469, L43
- Wallace, L., & Livingston, W., 1992, N.S.O. Technical Report #92-001
- Wallace, L., & Hinkle, K.H., 1996, *ApJS*, 107, 312
- Wallace, L., Livingston, W., Bernath, P.F., & Ram, R.S., 1998, N.S.O. Technical Report #1998-002
- Zapatero-Osorio M.R., Martín, E.L., Béjar, V.J., Bouy, H., Deshpande, R., & Wainscoat, R.J., 2007, *ApJ*, 666, 1205

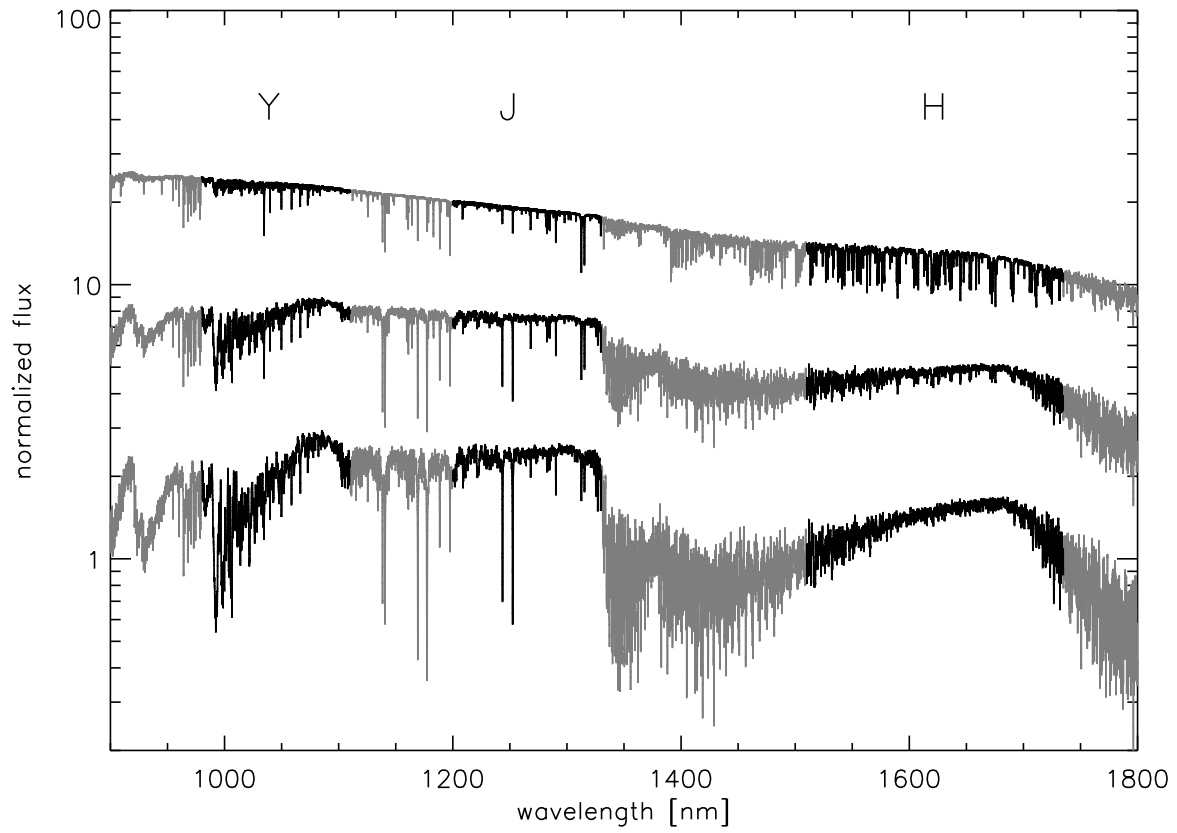


FIG. 2.— M star model spectra for three different effective temperatures: 3500 K (M3, upper panel), 2800 K (M6, middle panel), and 2400 K (M9, lower panel). The black regions show the photometric windows Y , J , and H . Gray regions are the telluric gaps separating these windows.

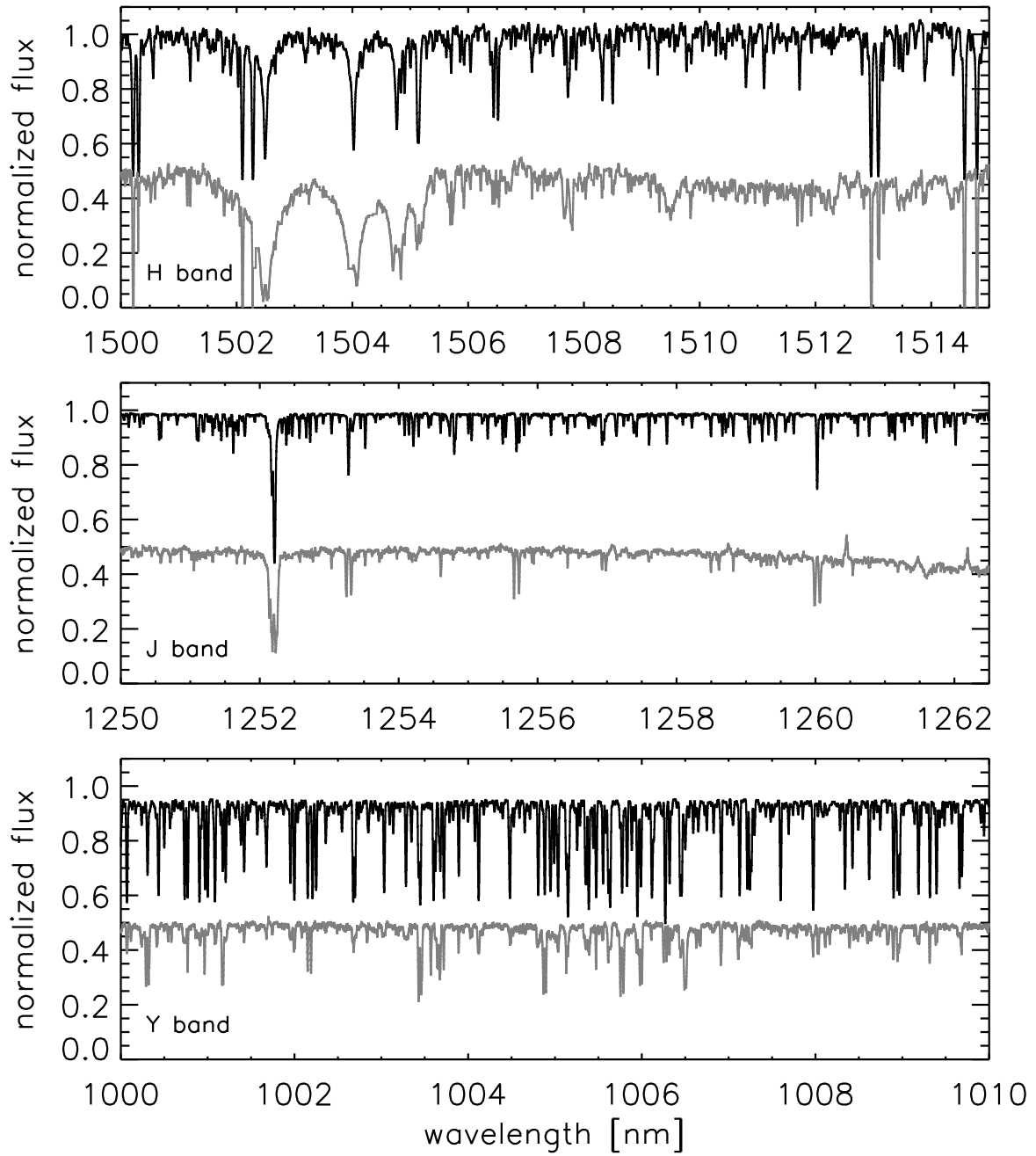


FIG. 3.— M star model spectrum for 3500 K (M3, black line) and a sunspot spectrum (grey line) in the *Y*-, *J*-, and *H*-bands.

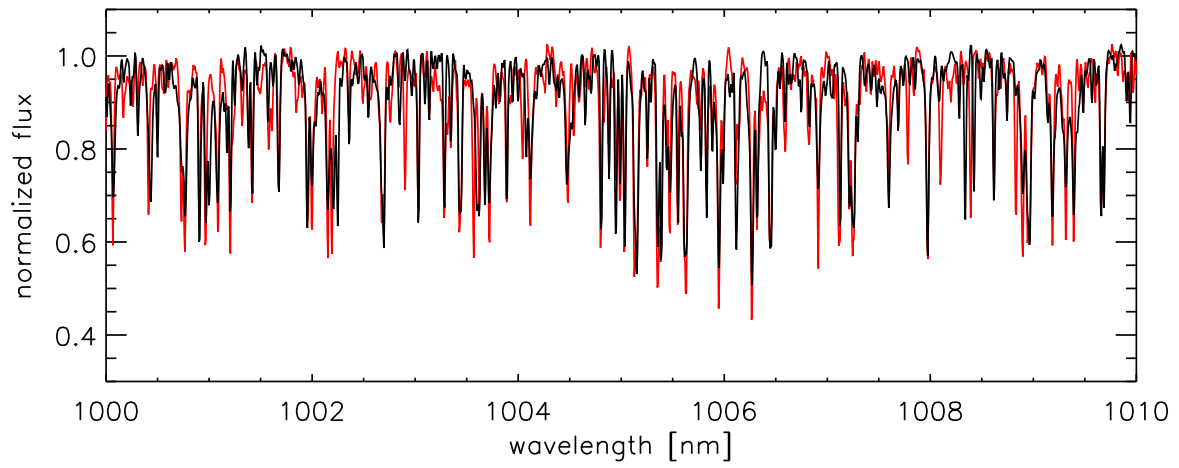


FIG. 4.— CRIRES spectrum of GJ 1002, M5.5 (red), and a model spectrum for $T=3200\text{K}$ and $\log g=4.75$ (black).

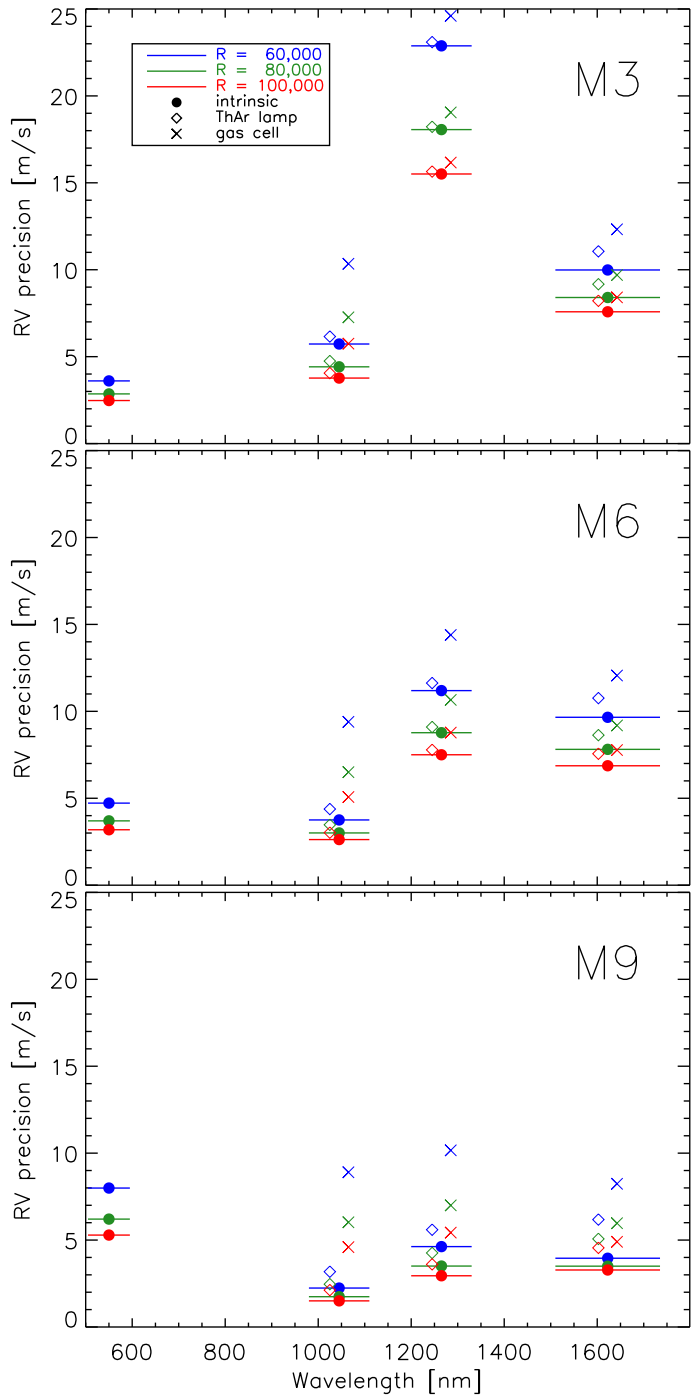


FIG. 5.— Radial velocity precision for 3500 K (M3, top panel), 2800 K (M6, middle), and 2400 K (M9, bottom). The situation is shown for three different spectral resolutions (red: $R = 100,000$; green: $R = 80,000$; blue: $R = 60,000$), S/N is scaled according to the spectral resolution and assuming constant instrument efficiency (see Table 2). Horizontal lines show the spectral coverage used for the calculation. Filled circles show the best achievable precision assuming perfect wavelength calibration, i.e., the intrinsic stellar information content. Open rhombs and crosses show the situation for wavelength calibration using ThAr lines and a hypothetical gas cell, respectively. In V , only the ideal case is shown because the wavelength calibration is not the limiting factor for the situations shown here.

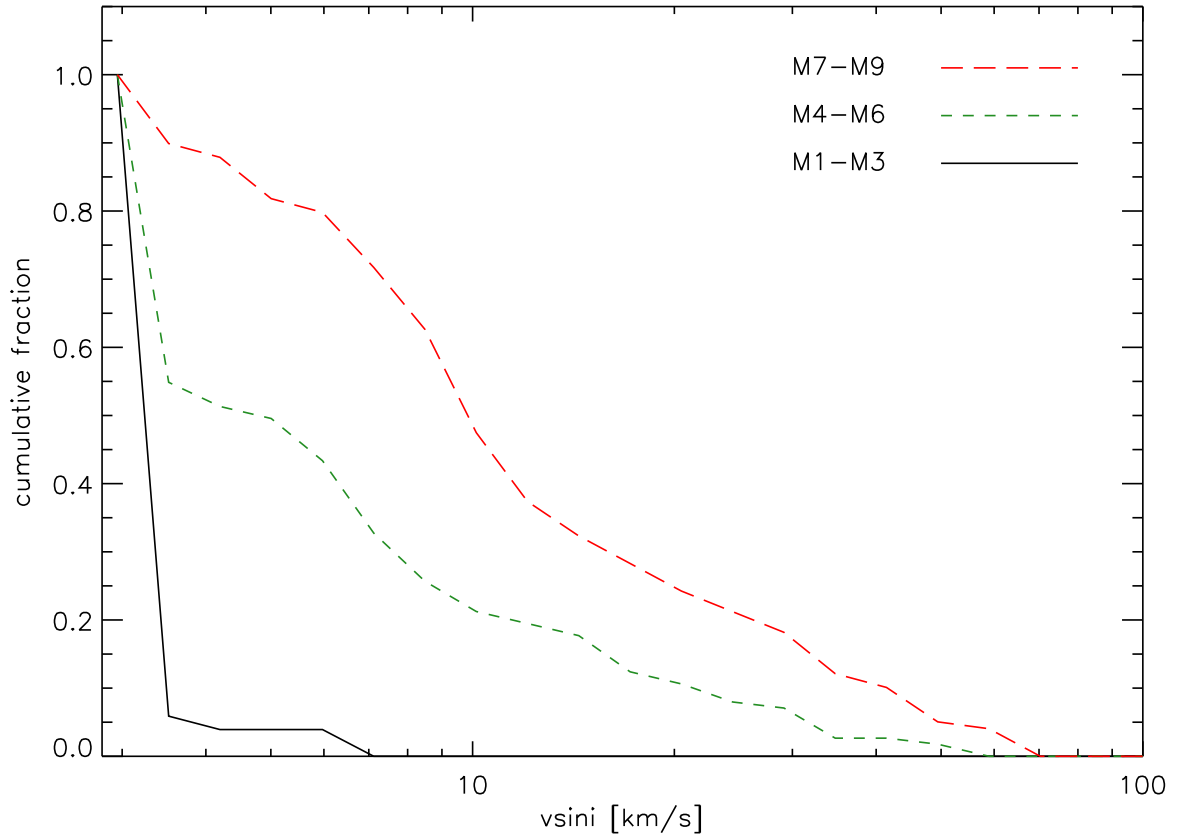


FIG. 6.— Distribution of rotational velocities among field M dwarfs. Cumulative plot showing the fraction of early-M (M1–3), mid-M (M4–M6), and late-M (M7–M9) stars rotating faster than a given value of $v \sin i$. Data are from Delfosse et al. (1998); Mohanty & Basri (2003); Reiners & Basri (2008) and Reiners & Basri (submitted to ApJ). A lower detection limit of $v \sin i = 3 \text{ km s}^{-1}$ is assumed for all data.

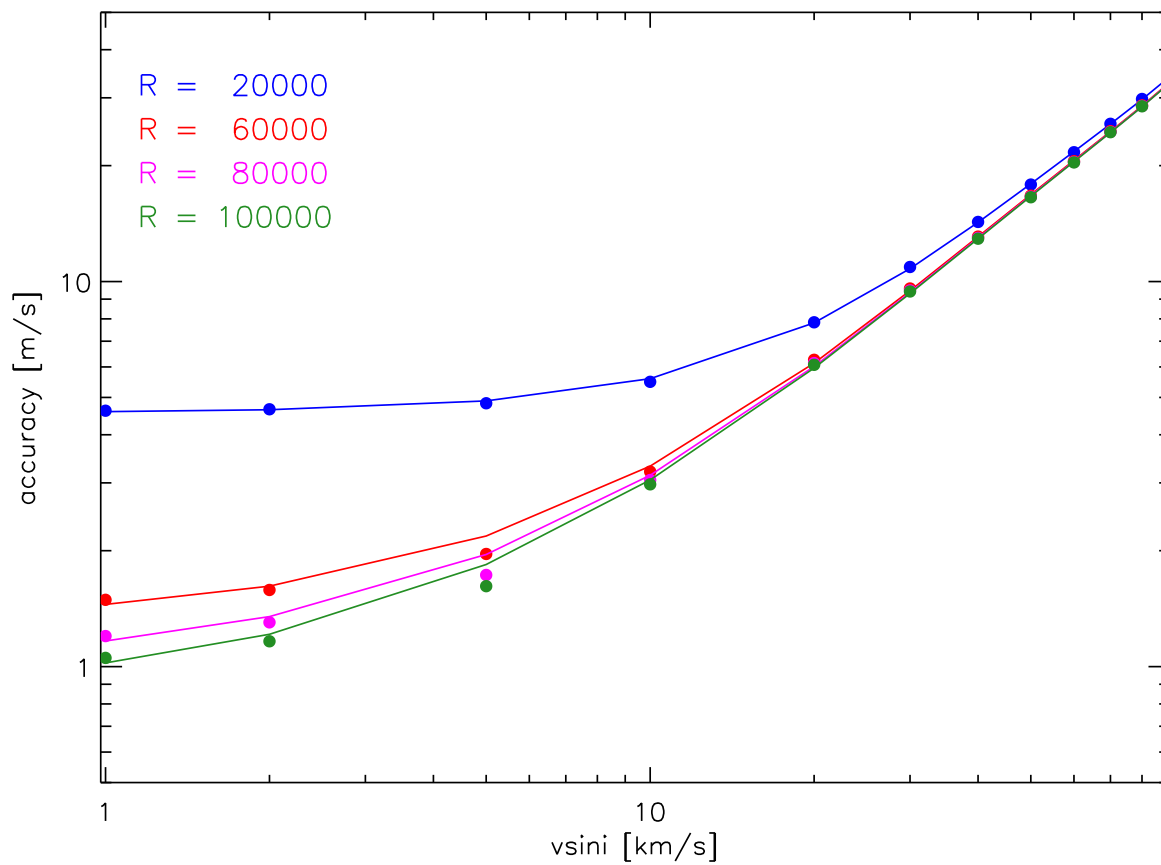


FIG. 7.— Radial velocity precision as a function of rotational velocity for four different resolving powers. The assumed model is a 3000 K star and the precision was calculated in the Y-band.

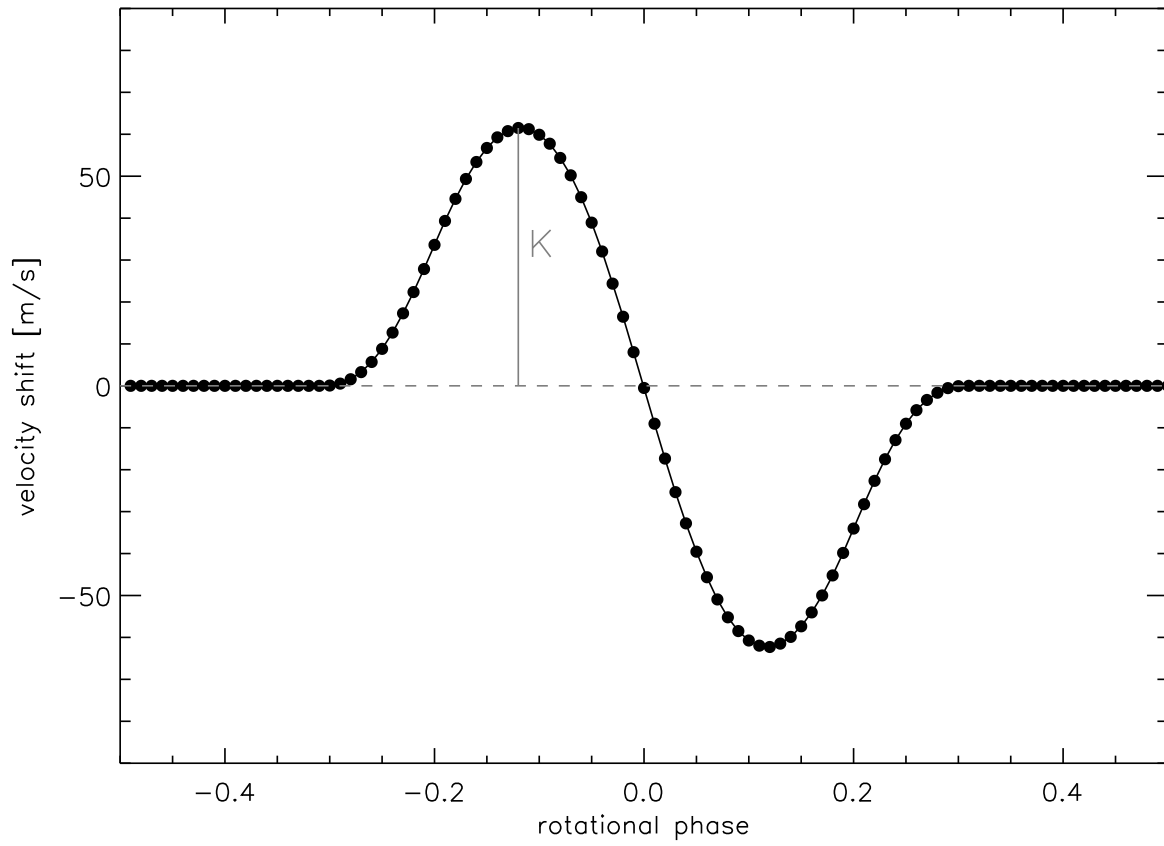


FIG. 8.— Example of the apparent radial velocity shift induced by a single cool spot as a function of rotational phase. Our assumed definition of the radial velocity amplitude, K , is indicated.

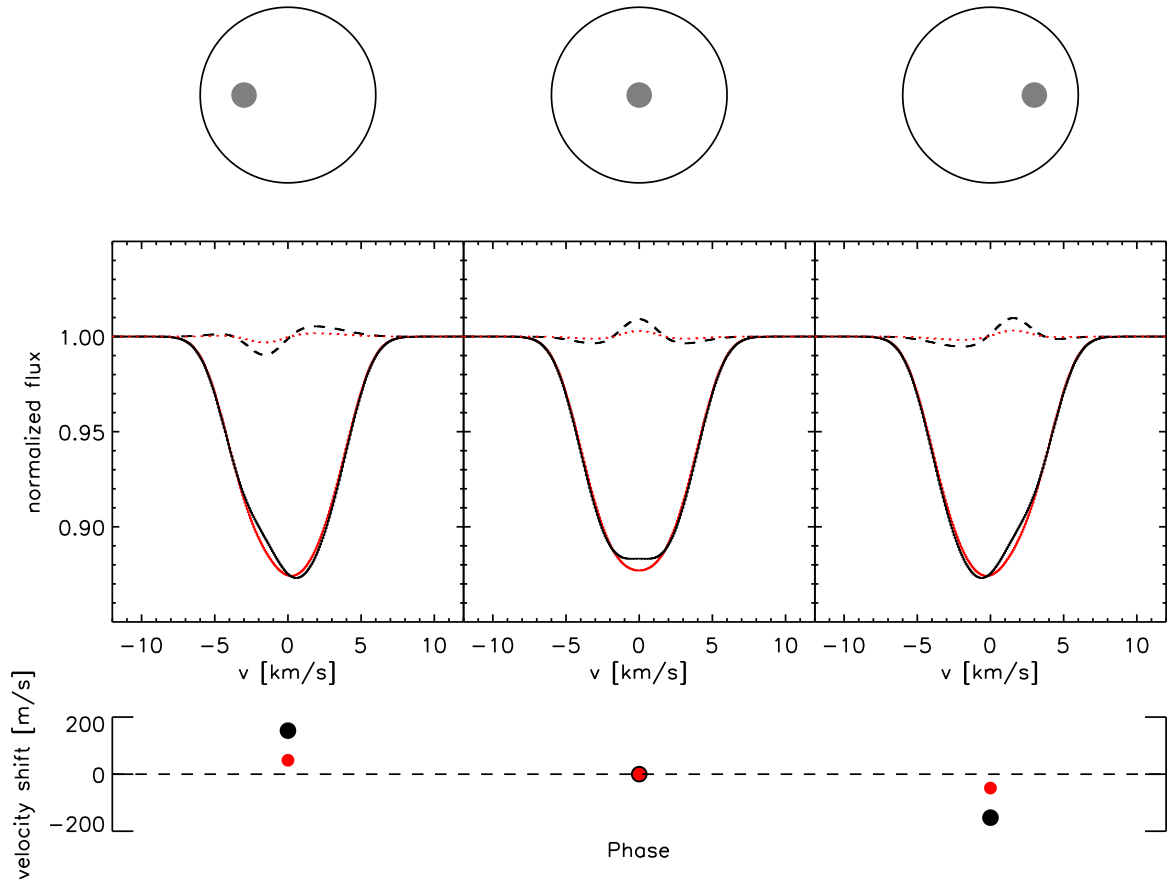


FIG. 9.— Illustration of the apparent radial velocity shift due to a single spot for two contrast values. From left to right, three different phases are shown, the top panel illustrates the location of the spot at each phase. The center panel shows line profiles (solid lines) and residuals (dashed lines; residual between the profile of the quiet photosphere and the profile of the spotted star) for a star with a photospheric temperature of $T = 3700$ K rotating at $v \sin i = 5 \text{ km s}^{-1}$. Black and red lines indicate different spot temperatures (black: $T_{\text{spot}} = 0$ K, red: $T_{\text{spot}} = 3500$ K.). The lower panel shows the measured radial velocity shift.

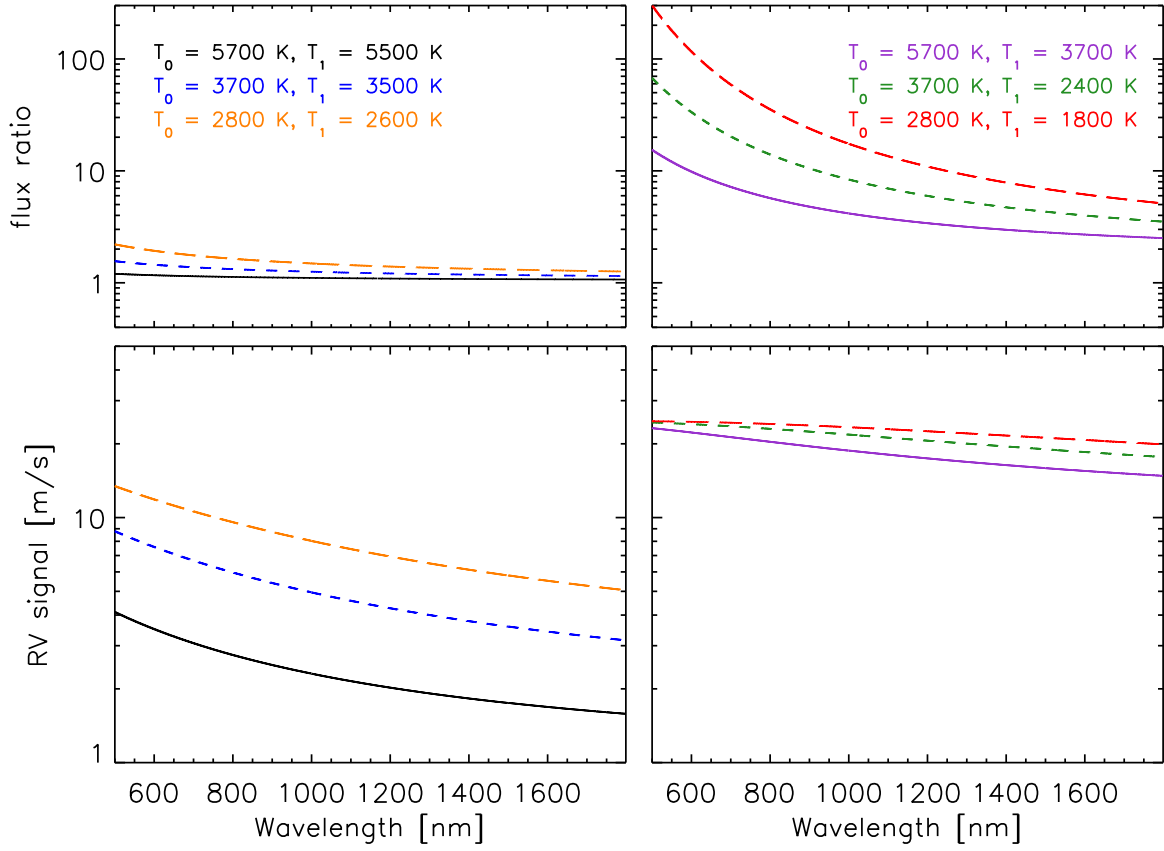


FIG. 10.— Apparent radial velocity shift by a single spot for different temperature contrasts calculated with our “toy model”. Upper panel: Flux ratio due to a cool spot with temperature T_1 on a surface at temperature T_0 , the contrast follows the ratio of the black-body distributions of the flux. Lower panel: Radial velocity signal induced by the spot during a rotation of the star at $v \sin i = 2 \text{ km s}^{-1}$. The left panel shows the situation of small contrast ($T_0 - T_1 = 200$ K), in the right panel the contrast is larger ($(T_0 - T_1)/T_0 = 0.35$).

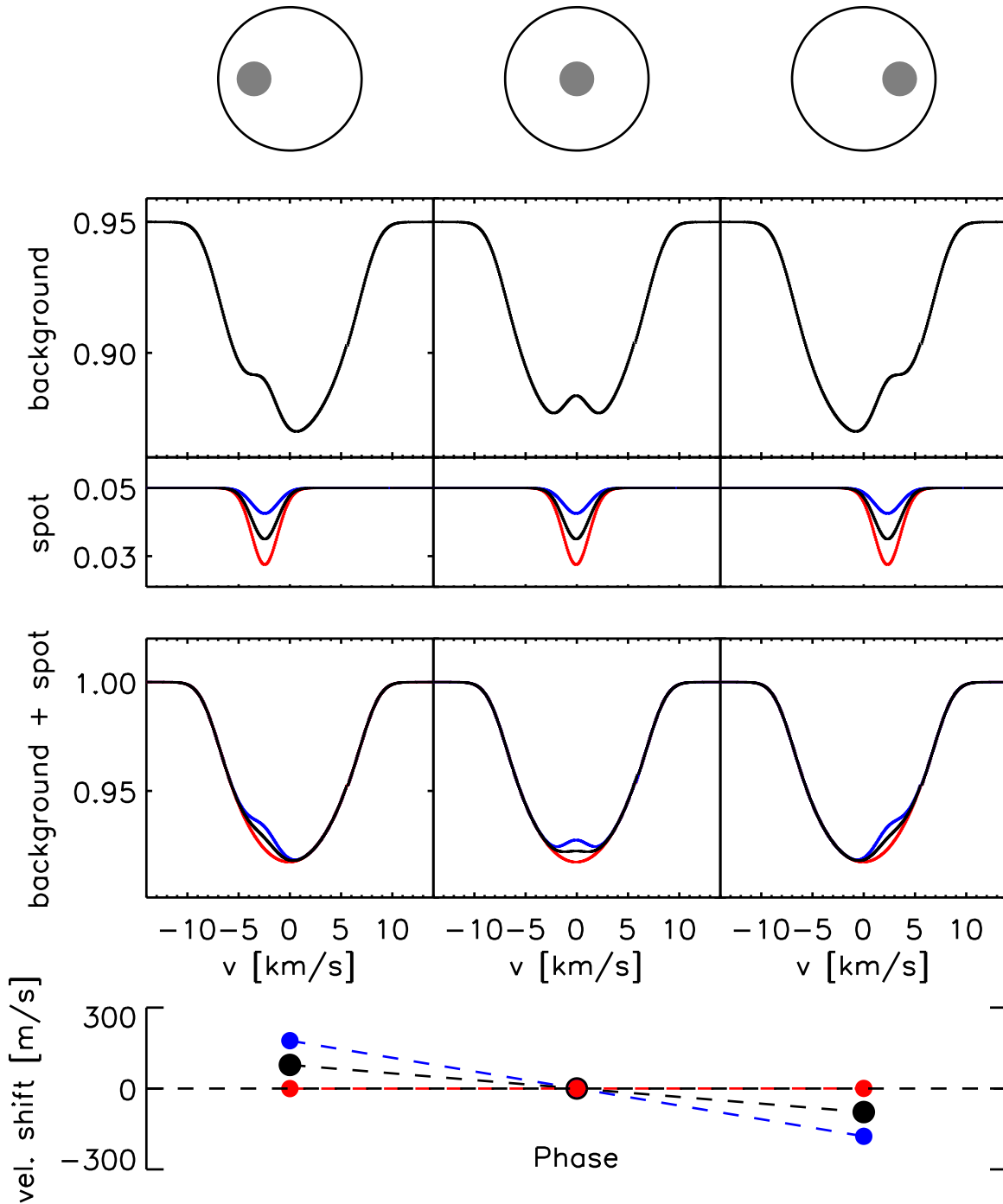


FIG. 11.— Illustration of apparent radial velocity shift by a single spot for different spot line intensities (toy model). The upper panel of the line profile plots gives the line profile contribution from the background photosphere. The middle panel gives the three different line profile contributions from a cool spot. The lower panel shows the sum of the two line profile contributions, i.e., the final spectrum of the spotted star for three cases of different spot line depths. The flux scale is normalized so that the total spectrum has a continuum value of 1, note the background continuum is at a value of 0.95 and the spot continuum at 0.05. The black line shows the case where the spot and background photosphere lines are identical. The bottom plot shows the resulting radial velocities for the different line profile combinations.

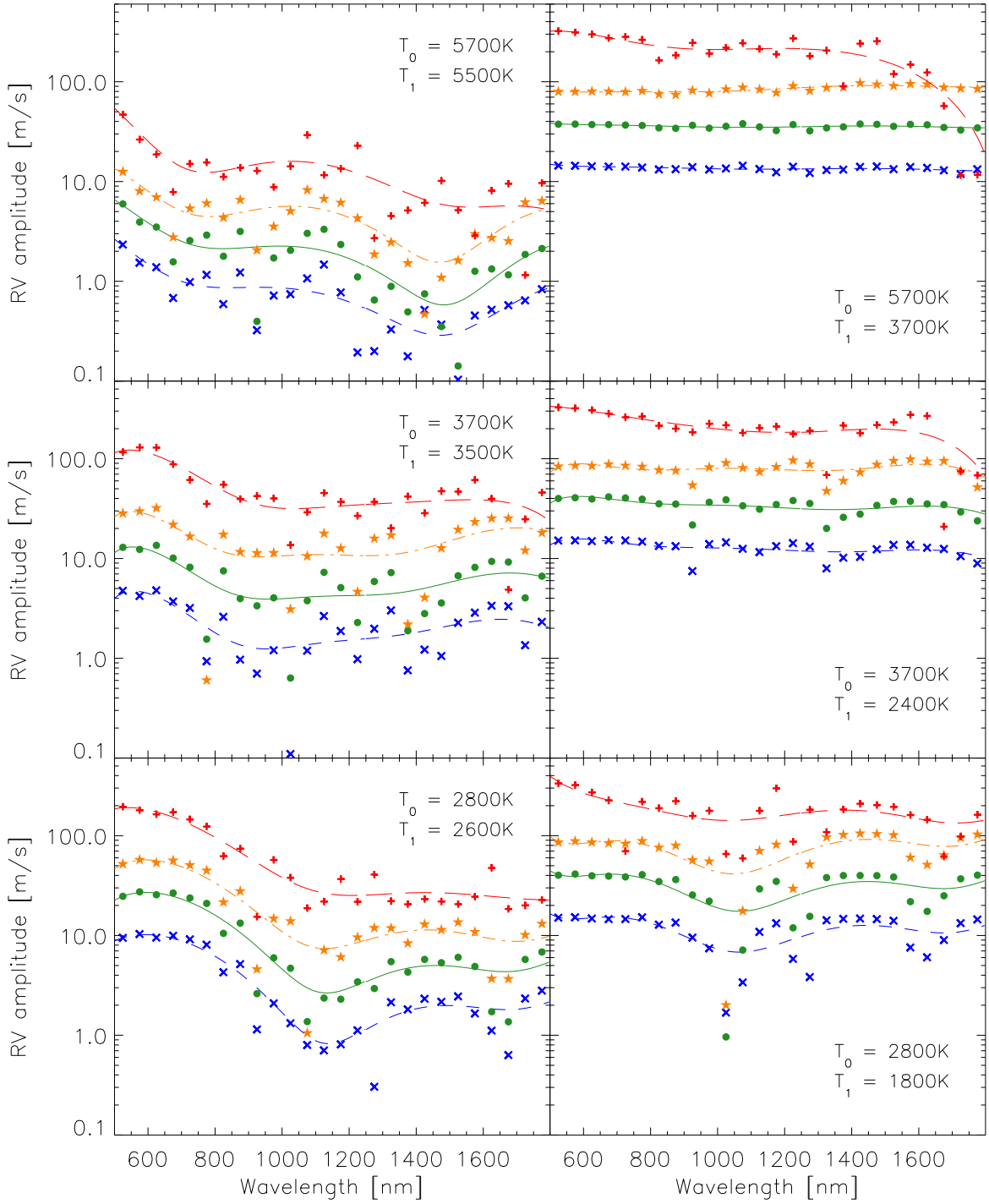


FIG. 12.— Simulations of RV amplitude as a function of wavelength for different temperature combinations and different rotation velocities. Individual points indicate the RV amplitude at one wavelength chunk, blue crosses are for $v \sin i = 2 \text{ km s}^{-1}$, green circles: $v \sin i = 5 \text{ km s}^{-1}$; orange stars: $v \sin i = 10 \text{ km s}^{-1}$; red pluses: $v \sin i = 30 \text{ km s}^{-1}$. Temperatures of the photosphere (T_0) and the spot (T_1) are shown in the panels. The spot has a size of 1% of the projected surface. Individual points are connected by a polynomial fit to guide the eye.